

## Littoral blasts: Pumice-water heat transfer and the conditions for steam explosions when pyroclastic flows enter the ocean

J. Dufek,<sup>1</sup> M. Manga,<sup>1</sup> and M. Staedter<sup>1</sup>

Received 19 December 2006; revised 30 June 2007; accepted 26 July 2007; published 16 November 2007.

[1] Steam explosions, or littoral blasts, generated when pyroclastic flows interact with seawater may be a common, although rarely documented, phenomena. The development of steam explosions rather than passive steam production is related to the rate of thermal energy transfer from hot pyroclasts to water. We conduct a series of laboratory experiments to quantify the heat transfer and steam production rates when hot pyroclasts encounter water. Hot pumice ( $>200^{\circ}\text{C}$ ) rapidly ingests water while remaining at the surface, producing measurable amounts of steam during the process. Approximately 10% of the thermal energy of the pumice particles is partitioned into the production of steam, and smaller particles have greater steam production rates. The laboratory experiments are used to develop a subgrid model for steam production that can be incorporated into a multiphase numerical framework. We use this model to study the critical steam production rates required to initiate explosive events. For conditions typical of many pyroclastic flows, particles smaller than  $\sim 1\text{--}5\text{ mm}$  are required to initiate a littoral blast. A second set of two-dimensional numerical simulations is conducted to simulate the 12–13 July Soufrière Hills dome collapse event that reached the sea. The simulations predict that the focus of the blast is likely generated several hundred meters offshore and although the landward directed base surge is primarily dry ( $<15\%$  water vapor), the area immediately above the blast is steam-rich and may be a likely site for the production of accretionary lapilli.

**Citation:** Dufek, J., M. Manga, and M. Staedter (2007), Littoral blasts: Pumice-water heat transfer and the conditions for steam explosions when pyroclastic flows enter the ocean, *J. Geophys. Res.*, 112, B11201, doi:10.1029/2006JB004910.

### 1. Introduction

[2] The widespread occurrence of many volcanic edifices in proximity to Earth's coastlines has resulted in numerous eruptive flows that have interacted with water. Pyroclastic flow deposits of the Kos, Krakatau, and Campanian eruptions on distant landmasses demonstrate that eruptive flows can sometimes travel considerable distances ( $>40\text{ km}$ ) over water [Allen and Cas, 2001; Carey et al., 1996; Fisher et al., 1993]. More commonly, eruptive flows that reach the sea have only proximal interaction with water. Eyewitness accounts and proximal deposits have documented the potentially explosive interaction when hot pyroclastic flows encounter liquid water [Edmonds and Herd, 2005; LaCroix, 1904; Sigurdsson et al., 1982], yet little is known about the precise criteria for the generation of littoral blasts and their associated facies. It may be that littoral blasts are a common occurrence in pyroclastic flows that reach water, but that deposits have either been poorly preserved or have been previously overlooked due to their limited exposure. Recently, dome collapses of Soufrière Hills volcano, Montserrat have produced pyroclastic density currents that

reached the sea [Edmonds and Herd, 2005]. These dome collapse events provide an opportunity to study the dynamics of flows as they first enter the water.

[3] Upon reaching the sea, pyroclastic density currents can interact in a number of ways with a water substrate (Figure 1). The most obvious interaction is the enhanced loss of particles at the air-water interface where saltation is relatively inhibited compared to land surfaces [Dufek and Bergantz, 2007]. The inertial coupling of the wind and water [Bye, 1995; Taylor and Gent, 1978] may also play a role in the mass transfer of particle-laden flows after they have traveled a considerable distance over water. The thermal energy transfer from hot flows to the water substrate may also be an important difference between over-land and over-water flows [Allen and Cas, 2001; Freundt, 2003; Watts and Waythomas, 2003]. Passive steam production resulting in elutriation of fine particles and violent steam explosions (littoral blasts) have both been hypothesized to result from these interactions [Allen and Cas, 2001; Edmonds and Herd, 2005]. Much has been learned from a number of magma-water interaction experiments [Grunewald et al., 2007; Zimanowski et al., 1997], yet the specific physical and thermodynamic controls on the heat transfer and on the conditions for steam explosions from pyroclastic flows have not been fully explored.

[4] The most vigorous pumice-water interaction is likely to occur where the volcanic flows are hottest, in proximal

<sup>1</sup>Department of Earth and Planetary Science, University of California, Berkeley, California, USA.

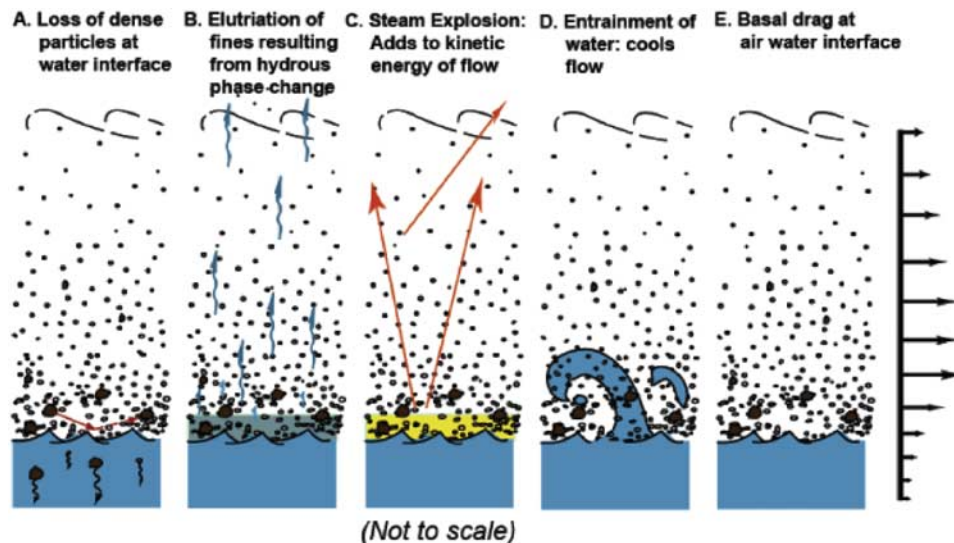


**Figure 1.** Schematic representation of the potential interactions between a pyroclastic flow and water.

locations where pyroclastic density currents first interact with water. An example of such a situation occurred during the 12–13 July 2003 dome collapse of Soufrière Hills. *Edmonds and Herd* [2005] described a new facies produced by a landward directed base surge as the dome collapse material entered the water. The resulting steam explosion produced a base surge that traveled as much as 4 km inland and up to 300 m in elevation. Analogue experiments have also shown the potential for steam explosions as pyroclastic density currents enter the water. *Freundt* [2003] conducted a series of experiments in which heated ash was dropped onto an inclined ramp that directed the flow to a water reservoir. Steam explosions were observed when the temperature of the ash was greater than 250°C. These experiments also described a bifurcation in the flow as it entered the water with the more dilute upper parts of the flow forming outgoing surges and the more dense, basal regions of the flow forming submarine currents.

[5] Prediction of steam explosions requires accounting for the multiphase heat transfer between the volcanoclastic particles and liquid water. Several multiphase heat transfer models have been advanced in the fields of chemical and nuclear engineering over the last 30 years [*Gunn*, 1978; *Zabrodsky*, 1963]. These approaches commonly develop an empirical heat transfer coefficient for the mean heat transfer from the dispersed phase to the fluid.

[6] There are several indications that in addition to the mean heat transfer relations, a local, or subgrid, model is needed to account for the heat transfer and vaporization at the scale of individual particles. This arises because numerical simulations and experiments, to a certain extent, are often limited to spatial and temporal resolutions greater than those that govern small-scale phenomena surrounding individual particles. The clearest indication of the need for a subgrid relation can be illustrated by a simple experiment. When one drops a pumice particle that is heated to several hundred degrees C into a beaker of water, it will remain at the surface for a finite period of time over which it will heat a small local volume of water and produce an amount of steam. This particle will then sink (often within seconds) as it ingests water into its pore space. If the temperature of the

beaker of water is measured it will be considerably below the boiling temperature of water as the thermal energy from the pumice has been spread by convection throughout the beaker. From the standpoint of looking at the mean temperature of the water in the beaker there is an apparent paradox where phase change has occurred but the temperature of the water is far from its boiling temperature; however this is only a reflection of the scale of the measurement.

[7] In this paper we develop a model to reconcile steam production at small scales with the overall thermal budget of pyroclastic flows. We describe the results of laboratory experiments on the steam production and heat transfer of pumice to water. These experiments are then linked to macroscale dynamics via a multiphase numerical model [*Agrawal et al.*, 2001; *Dufek and Bergantz*, 2007]. We introduce a subgrid-scale model to predict steam production of pumice particles near the water surface, and present a scaling argument for the necessary steam production rates to produce steam explosions in pyroclastic flows. Finally, numerical simulations are conducted to analyze conditions similar to those during the Montserrat littoral blast event.

## 2. Experimental Methods

### 2.1. Experimental Determination of Heat Transfer and Steam Production

[8] We performed heat transfer experiments to elucidate the partitioning of enthalpy between latent and sensible heat as pumice interacts with water. These experiments were conducted with pumice particles and glass beads that lack the internal porosity of the pumice. In all experiments the pumice is from pyroclastic deposits of Medicine Lake Volcano in northern California, with an average density of  $550 \pm 39 \text{ kg/m}^3$  and bubble size mode smaller than 1 mm [*Cagnoli and Manga*, 2004]. A range of particle sizes was used in the experiments as described in auxiliary material Table S1 and Figure 2, and the temperature range examined was between 100 and 700°C.<sup>1</sup>

<sup>1</sup>Auxiliary materials are available at <ftp://ftp.agu.org/apend/jb/2006/jb004910>.

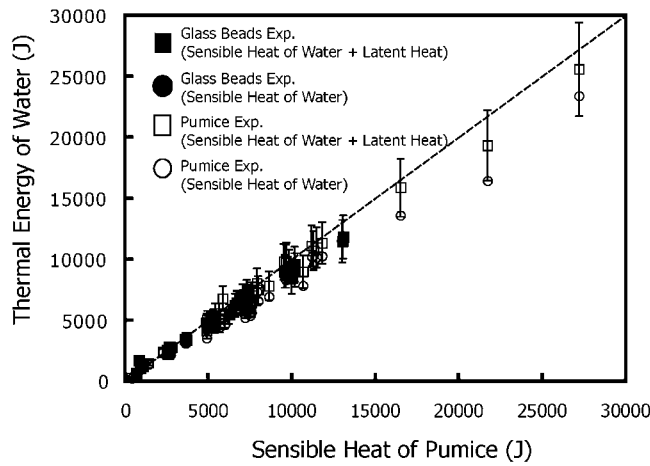


**Figure 2.** Initial sensible heat of the pumice (in joules) compared to the final thermal energy of water and steam (in joules). Error in the sensible heat of pumice measurements (horizontal error bars) is smaller than the size of the symbols. Open symbols denote pumice, and solid symbols denote glass beads. Circles refer to the sensible heat of the water, and squares denote both the sensible heat of the water plus the calculated latent heat from steam generation. The dashed diagonal line represents the ideal energy balance if all thermal energy is accounted for in the experiments. The total thermal energy from the experiments (squares) is shown with 15% error bars.

[9] The first set of experiments was designed to examine the net heat transfer and steam production when pumice particles are dropped in water. Pumice and glass beads were heated in crucibles in a Lindberg furnace for several hours to attain thermal equilibrium. The particles were then immediately transferred to a Styrofoam container containing between 100 and 300 mL of water. The transfer time between the furnace and introduction into the water was less than 2 s. During this short transfer period the particles remained in already hot crucibles to further minimize cooling during transfer. We measured the surface temperature of the crucibles in a subset of experiments using an Omega infrared thermometer. For the timescale of the transfer, no change in temperature difference could be measured within the accuracy of this device. A surface temperature decrease of 10°C required greater than ~6 s. Therefore we estimate that the surface cooling of the crucible over the transfer timescale was probably less than 2°C and contributes less than a percent error on our total energy budget. The mass and temperature of the water were measured both before and after the experiment to assess the amount of thermal energy transferred to the water and the mass of steam produced. Mass measurements were performed on a digital Ohaus scale with 0.001 g accuracy, and measurements were made immediately after the experiment to insure little loss of water due to evaporation. These experiments were designed to test the interaction with water of hot pumice filled with atmospheric gases (rather than primary magmatic gases). This is justified for pumice particles that have traveled some distance subaerially from the vent before reaching a water source and have had time for gas replacement. Combining Darcy's law with an estimate of dynamic

pressure driving gas flow through the particle ( $\frac{\rho \Delta u^2}{2}$ ), the gas replacement time can be estimated as  $t_{replace} \approx \frac{2\mu_{gas}d^2}{\kappa\rho_g\Delta u^2}$ , where  $\mu_{gas}$  is the gas viscosity,  $\rho_g$  is the gas density,  $\kappa$  is the pumice permeability,  $d$  is the pumice diameter, and  $\Delta u$  is pumice-gas differential velocity. Assuming a relative velocity between a pumice and the gas phase of 10 m/s and pumice permeability of  $10^{-12} \text{ m}^2$  [Klug and Cashman, 1996; Muller et al., 2005; Rust and Cashman, 2004; Saar and Manga, 1999] for a 1 cm diameter pumice the gas replacement time is ~20 s. On the basis of the saturation mechanisms discussed later, similar heat transfer rates and steam production rates are likely even if the pumice was still filled with primary magmatic gases.

[10] The measurements in the experiment can then be used to determine the thermal budget of the pumice-water system using the following relation:

$$^p m^p \bar{c}_p^p \Delta T = \Delta^w m^w L + ^w m^w c_p^w \Delta T. \quad (1)$$

Here the superscript  $w$  refers to water and  $p$  refers to particles. The mass is denoted by  $m$ , average heat capacity  $\bar{c}_p$ , latent heat of vaporization  $L$ , and the change in temperature by  $\Delta T$ . We define average heat capacity of pumice as

$$^p \bar{c}_p = \frac{1}{\Delta T} \int_{T_0}^{T_0 + \Delta T} ^p c_p(T) dT. \quad (2)$$

[11] This energy balance is based on the assumption that the mass of water that changes sensible heat is approximately constant, which is a reasonable assumption provided  $^w \Delta m / ^w m \ll 1$ . Moreover, we assume that  $\Delta^w m$  is caused by phase change from water to steam. Small loss of water due to evaporation or the occasional drop of water leaving the system could occur; to remove these biases from our results, we only considered as valid those results where the right-hand side of the conservation of energy equation (1) was within 15% of the left-hand side.

[12] A crucial component of the energy balance is the temperature-dependent heat capacity of the pumice. We used the composition- and temperature-dependent heat capacity data from Stebbins et al. [1984], along with the glass composition [Grove and Donnelly-Nolan, 1986] to determine the following relation for the pumice:

$$^p c_p(T) = 1.0567 + 2.0 \times 10^{-4}(T) - 3.84 \times 10^{-4}(T^2). \quad (3)$$

[13] The sensible heat of the particle ( $^p \Delta Q$ ) is then determined by integrating over the change in temperature of the particles to obtain the following relation:

$$^p \Delta Q = ^p m \times ([1.0567][T_f - T_i] + [85.326 \times 10^{-6}] \cdot [T_f^2 - T_i^2] + [38.437 \times 10^3][T_f^{-1} - T_i^{-1}]) \quad (4)$$

## 2.2. Constraining the Rate of Steam Production

[14] As observed by Whitham and Sparks [1986], hot pumice sinks very quickly compared to pumice at room temperature. In a separate set of experiments we quantify this effect by measuring the sinking time of hot pumice of



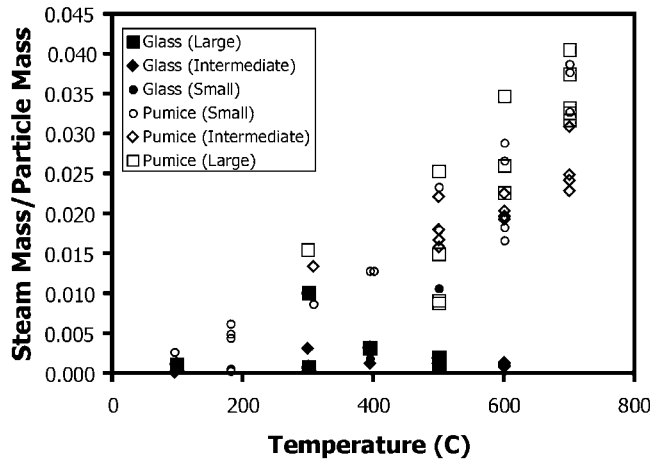


**Figure 3.** Steam production normalized by particle mass versus initial temperature of the pumice particles. The sizes of the particles are denoted by the symbol shapes and are binned as large pumice (12.5–15 mm diameter), intermediate pumice (8–9.5 mm diameter), small pumice (5–6 mm diameter), large glass beads (10 mm), intermediate glass beads (6 mm diameter), and small glass beads (2 mm diameter). The error bars are smaller than the size of the symbols.

various sizes using high-speed video (800 frames per second) to obtain accurate floating times for these pumices.

### 3. Experimental Results

#### 3.1. Sensible and Latent Heat Partitioning During Pumice Water Interaction

[15] The results of the particle-water heat transfer experiments are summarized in Figures 2–4 and in Table S1. Only

those experiments in which the total energy balance is within 15% of that accounted for by equation (1) are included (Figure 2).

[16] A result of these experiments is that glass beads produced almost no steam whereas pumice particles of similar mass and temperature produced measurable amounts of steam (Figure 3). When the glass beads were dropped into water they sank immediately, whereas the hot pumice remained at the surface while ingesting water before sinking.

[17] The mass of steam produced per pumice-water interaction depended on both the mass and temperature of the pumice particle. As Figure 3 illustrates the hotter particles systematically produced greater amounts of steam per mass of pumice. Figure 4 shows a nearly linear relationship is observed between the initial energy of the pumice particles,  $m_p c_p [T_i - T_w]$ , and the mass of steam produced.

#### 3.2. Rate of Water Ingestion

[18] We quantified the time a piece of pumice remains at the surface (i.e., has bulk density less than water) using high-speed video. The time at the surface can then be converted into an average rate of water ingestion. We note that the water ingestion rate may not be a linear function of time, and these measurements only can discern the average ingestion rates from initial placement in water until they reach the critical saturation for sinking.

[19] Systematic trends were observed related to the size of the pumice particle (Figure 5). Larger particles remained at the surface for a greater period of time and the relationship is nearly linear with a best fit slope of 3.595 s/g with  $r^2$  of 0.91. We note that surface tension effects become relevant for particle sizes below  $\sim 1.0$  mm and may be responsible

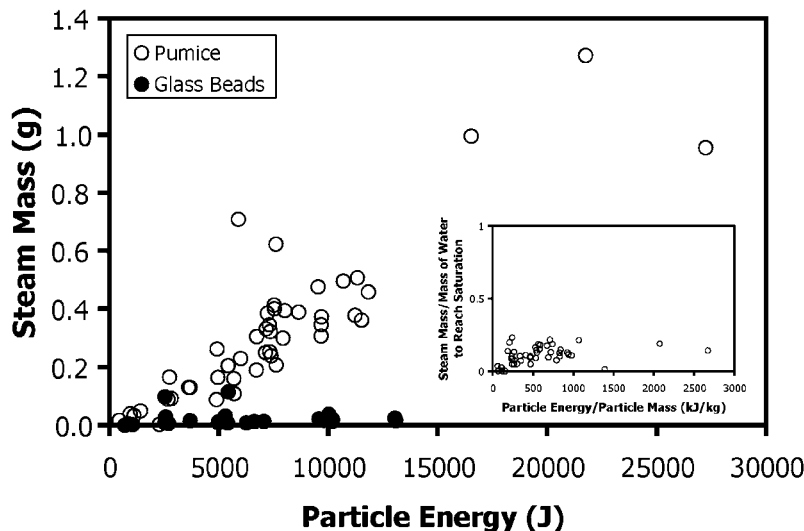


**Figure 4.** Initial particle energy (J) versus the net mass of steam produced (g). Open circles denote pumice particles, and shaded circles represent glass bead measurements. The glass beads produce almost no mass of steam, while the pumice particles produce a nearly linear array of mass of steam for given initial energy. A linear regression fit to the pumice particles yields a slope of  $4.44 \times 10^{-5}$  g/J with an  $r^2$  value of 0.886. Error bars are smaller than symbols used. Inset shows mass of steam produced by pumice normalized by the calculated water required to sufficiently saturate the pumice so that they sink (based on a porosity of 0.74).

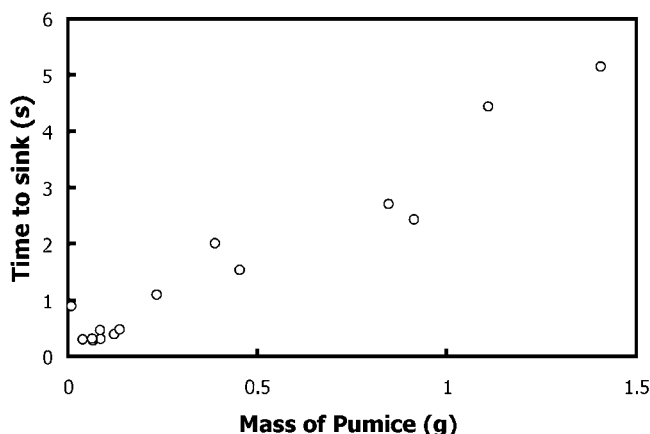


**Figure 5.** Mass of pumice (g) versus saturation time (s). The slope of the fit ( $\xi$ ) is  $\sim 3.595$  s/g (3595 s/kg) at  $T = 500^\circ\text{C}$ .

for the slightly greater timescales for the smallest particles [Kundu, 1990].

[20] We conducted an experiment to determine whether the liquid water that the pumice ingested was a result of steam condensation or of liquid water being drawn into the pumice. A beaker of water was dyed with food coloring and pumice particles at  $500^\circ\text{C}$  were placed so that only  $\sim 10\%$  of their volume was submerged in the water. Within the course of a couple of seconds colored water was drawn into the entirety of the pumice. This experiment was repeated for a number of masses and temperatures. Only at the ambient temperature is dyed water not drawn into the pumice (nor are steam production and condensation factors).

#### 4. Discussion of the Pumice Saturation Mechanism

##### 4.1. Hydrodynamic Instability

[21] The dyed liquid water entering the pumice illustrates that at least some water in liquid form must be drawn into the pumice. However, this test does not rule out the possibility of concomitant steam condensation. Liquid water ingestion could either be accomplished through contraction of the gas in the pumice due to cooling [Cashman and Fiske, 1991; Manville et al., 2002; Whitham and Sparks, 1986], or due to hydrodynamic instabilities where steam drives droplets into the pore space of the pumice. If the pumice is at the surface, contraction of gas due to cooling may also draw in ambient gas, perhaps more readily than water, whereas in submerged pumice gas-contraction-driven-saturation may be a more efficient mechanism. Likewise, significant water ingestion and sinking appears to only occur when there is measurable steam production. This is consistent with the steam production process being related to water ingestion.

[22] We heated glass tubes (inner diameters 6–10 mm) to  $500^\circ\text{C}$  and filmed their interaction when partially submerged in water with high-speed video to better visualize how phase change may accelerate the water ingestion

process. Representative dynamics of the water and steam mixture internal to the glass tube are shown in Figure 6.

[23] When placed in the water, vigorous steam production occurs both internal and external to the glass tube. In the inside of the tube the water-gas interface is extremely irregular due to steam production. We suggest that a Richtmyer-Meshkov instability is likely occurring where high-pressure gradients due to the phase change are misaligned with density gradients at the water surface [Brouillette, 2002]. This occurs because there is naturally some curvature in the water interface internal to the tube. The same effect would also occur internal to a pumice particle, but may be even more emphasized due the irregular surfaces of the pumice. A generalized Richtmyer-Meshkov instability develops when a shock wave interacts with the interface of two fluids, amplifying initial perturbations at the interface. In the case of the glass tube experiments, owing to the rapid expansion of steam, the instability grows as regions of water are preferentially forced down the tube, particularly near the annular regions; near the core, water is forced up. Water droplets produced in this manner are then forced up the tube as gas surrounding or behind the droplets expands and accelerates. This results in quasiperiodic build of pressure and ejection of water droplets that produces an audible popping noise. For the smaller diameter tubes the escaping gas appeared to preferentially develop larger bubbles pushing water in front of it (in some cases in a slug flow regime). We note that even the smallest diameter tube used is about an order of magnitude greater than the submillimeter porosity structure of the pumice [Cagnoli and Manga, 2004]. At vesicle scales, surface tension of water will have an even greater effect. Experiments conducted on microtubules ( $\sim 0.3$  mm and smaller) show that under these conditions flow boiling almost always occurs in slug flow regime, and the expanding gas can push water in front of it [Kandlikar and Balasubramanian, 2005].

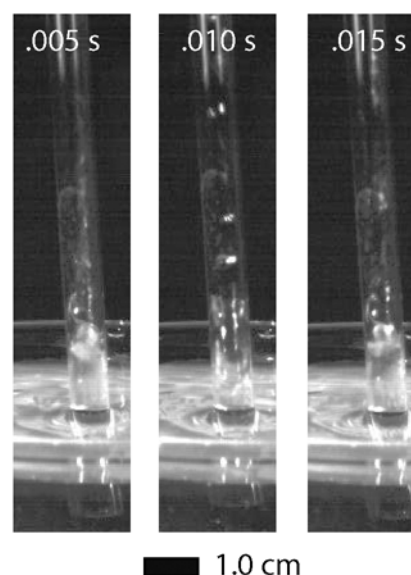


**Figure 6.** Hydrodynamic instability when hot ( $500^\circ\text{C}$ ) glass tube is placed in water. The glass tube is 6 mm in diameter.

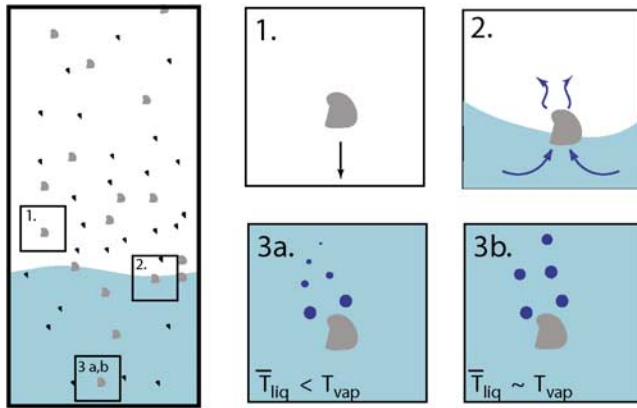


**Figure 7.** Schematic representation of the stages of heat transfer from pumice particles to water that generate steam. The amount of heat transfer is ultimately governed by the rate of particle deposition onto the water surface (stage 1). At the water surface, steam is produced around the pumice, driving rapid ingestion of water (stage 2), as the pumice sinks it can still potentially produce steam, but if the water is below the boiling temperature ( $T_{vap}$ ), it will condense and not contribute to the net steam in the atmosphere.

[24] Although the ingestion of water into pore space via hydrodynamic instability seems a plausible mechanism for pumice saturation, we note that other small-scale mechanisms may also produce rapid interaction and phase change. For instance, fragmentation of volcanic material as it interacts with the water surface will rapidly increase the surface area available for heat transfer [Wohletz, 1986]. Both secondary fragmentation and ingestion of water into pore space produce a large surface area for heat transfer, and increases the rate at which heat can be transferred to the water. Likewise, the production of fine water drops that are entrained in the flow may also result in rapid phase change, although the details of this process are beyond the scope of this study.

#### 4.2. Efficiency of the Saturation Mechanism

[25] Elevated temperature, steam production and enhanced water ingestion are all likely part of a self-consistent process of a steam-driven water ingestion mechanism. This is one potential reason why there is a nearly a linear relationship between the amount of steam produced and the size of a particle; steam production will continue until the pumice is sufficiently saturated to sink. By this conjecture, only steam needed to drive water into the pumice (minus some loss of steam that does not drive any liquid water) will be recorded in the net steam production calculation. Once below the surface, phase change may continue to occur, but because the mean temperature is below the water boiling temperature the rising steam will mostly condense before reaching the surface (Figure 7). This explains why glass beads, while having as much or more thermal energy per unit volume compared to the pumice, produce nearly no net steam. Because they do not remain at the surface, any steam that is produced locally around the glass bead condenses before making any contribution to the atmosphere. Of course, after

the column of water has reached its boiling temperature any steam produced by a particle will contribute to the net steam budget.

[26] The linear relationship between particle thermal energy and mass of steam produced can be described in terms of the efficiency of the heat transfer process. If all the thermal energy from a particle is concentrated on only the water that produces steam, the expected values in Figure 4 would be given by

$$^vm = \frac{^pE}{^wc_p\Delta^vT + ^vL}, \quad (5)$$

where  $^pE$  is the thermal energy of the particle,  $^wc_p$  is the heat capacity of the water,  $\Delta^vT$  is the change in temperature of the water from its initial temperature to vapor temperature, and  $^vL$  is the latent heat of vaporization. For typical conditions in the experiments the slope would be given by  $1/^wc_p\Delta^vT + ^vL$  and would have a value of  $\sim 0.00039$  g/J. The measured slope is  $\sim 4.44 \times 10^{-5}$  g/J, demonstrating that the process is only about 10% efficient at producing steam. We introduce the efficiency factor of  $^v\varepsilon$  with a value of 0.114, to fit the empirical result in Figure 4, so that

$$m_v = \left[ \frac{^v\varepsilon}{^wc_p\Delta T_v + ^vL} \right] ^pE. \quad (6)$$

## 5. Extension to Pyroclastic Flow Scales

### 5.1. A Subgrid Model for Steam Production

[27] We develop a subgrid model for steam production to extend the pumice-scale laboratory measurements to predictive models of macroscopic pyroclastic flow behavior. The subgrid model is developed in the context of multiphase continuum theory. In the continuum multiphase approach separate equations for mass, momentum, and thermal energy are solved for each mechanically distinct phase. The separate phases are interpenetrating continua with volume fractions equal to unity in a control volume. In this study we adapt the MFIX (multiphase flow with interface exchanges) numerical approach to volcanic flows [Gera *et al.*, 2004]. This code has been verified for particle-laden gravity currents similar to the conditions studied here [Dufek and Bergantz, 2007]. For a detailed discussion of the model and validation we refer the reader to Dufek and Bergantz [2007] which used the same numerical scheme and granular and turbulence constitutive relations and particle-fluid drag relations. Similar approaches have been used to study the dynamics of collapsing columns, pyroclastic flow dynamics, and volcanic conduit dynamics [Darteville *et al.*, 2004; Dufek and Bergantz, 2007, 2005; Neri *et al.*, 2002].

[28] In the numerical simulations presented here, up to four separate phases are solved for including water, gas, and two particle phases each with a different particle diameter. We introduce the following set of equations to describe mass, momentum and thermal energy conservation.

**Table 1.** Nomenclature<sup>a</sup>

Parameter	Description	Value
$a$	speed of sound	m/s
$c$	characteristic velocity	m/s
$\bar{c}_p$	heat capacity	J/kg K
$^p d$	particle diameter	m
$E$	thermal energy	J
$\bar{H}$	mean interphase heat transfer	J/m <sup>3</sup> s
$H^s$	subgrid interphase heat transfer	J/m <sup>3</sup> s
$I$	interphase momentum transfer (drag)	Pa/m <sup>3</sup>
$^w k$	thermal conductivity	W/m K
$L$	specific latent heat of vaporization	J/kg
$m$	mass	kg
$P$	pressure	Pa
$q$	thermal heat flux	J/m <sup>2</sup> s
$\Delta Q$	change in sensible heat	J
$R_v$	steam production rate	kg/m <sup>3</sup> s
$R$	gas constant	J/K kg
$\bar{S}$	mean latent heat of vaporization	J/m <sup>3</sup> s
$S^s$	subgrid latent heat of vaporization	J/m <sup>3</sup> s
$T$	temperature	K
$U_i$	velocity	m/s
$\mathbf{x}$	spatial position	M
$X$	mass fraction	
$\alpha$	volume fraction	
$^v \varepsilon$	steam efficiency factor (0.114)	
$\gamma_{pw}^0$	heat transfer coefficient	
$\gamma$	ratio of heat capacities	
$\xi$	sinking coefficient	s/kg
$\rho$	density	kg/m <sup>3</sup>
$\tau_{ij}$	stress tensor	Pa
$Nu$	Nusselt number correlation	
$\frac{[7 - 10(^w \alpha) + 5(^w \alpha)^2] [1 + 0.7(\text{Re}_p)^2 (\text{Pr})^{.33}] + [1.33 - 2.4(^w \alpha) + 1.2(^w \alpha)^2] (\text{Re}_p)^7 (\text{Pr})^{.33}}{[1.33 - 2.4(^w \alpha) + 1.2(^w \alpha)^2] (\text{Re}_p)^7 (\text{Pr})^{.33}} +$		

<sup>a</sup>Superscripts:  $p$ , particle phases;  $w$ , water phase;  $v$ , water vapor. Subscripts  $i, j = 1, 2$  (indices for spatial direction).

[29] Continuity equations for the water, gas and particle phases are

$$\frac{\partial}{\partial t} (^w \alpha^w \rho) + \frac{\partial}{\partial x_i} (^w \alpha^w \rho^w U_i) = \underbrace{-R_v}_{\text{Mass loss due to phase change}}, \quad (7)$$

$$\frac{\partial}{\partial t} (^g \alpha^g \rho) + \frac{\partial}{\partial x_i} (^g \alpha^g \rho^g U_i) = \underbrace{+R_v}_{\text{Mass gain due to phase change}}, \quad (8)$$

and

$$\frac{\partial}{\partial t} (^p \alpha^p \rho) + \frac{\partial}{\partial x_i} (^p \alpha^p \rho^p U_i) = 0, \quad (9)$$

respectively. Similarly, the momentum equations for the water, gas and particle phases are given as

$$\begin{aligned} \frac{\partial}{\partial t} (^w \alpha^w \rho U_i) + \frac{\partial}{\partial x_i} (^w \alpha^w \rho^w U_i^w U_j) \\ = \frac{\partial^w P}{\partial x_i} \delta_{ij} + \frac{\partial^w \tau_{ij}}{\partial x_j} + ^w I_i + ^w \alpha^w \rho g_i - \underbrace{R_v^w U_i}_{\text{Momentum loss due to phase change}}, \end{aligned} \quad (10)$$

$$\begin{aligned} \frac{\partial}{\partial t} (^g \alpha^g \rho U_i) + \frac{\partial}{\partial x_i} (^g \alpha^g \rho^g U_i^g U_j) \\ = \frac{\partial^g P}{\partial x_i} \delta_{ij} + \frac{\partial^g \tau_{ij}}{\partial x_j} + ^g I_i + ^g \alpha^g \rho g_i + \underbrace{R_v^g U_i}_{\text{Momentum gain due to phase change}}, \end{aligned} \quad (11)$$

and

$$\frac{\partial}{\partial t} (^p \alpha^p \rho U_i) + \frac{\partial}{\partial x_i} (^p \alpha^p \rho^p U_i^p U_j) = \frac{\partial^p P}{\partial x_i} \delta_{ij} + \frac{\partial^p \tau_{ij}}{\partial x_j} + ^p I_i + ^p \alpha^p \rho g_i. \quad (12)$$

[30] The water, gas, and particle phase thermal energy conservation relations are

$$\begin{aligned} ^w \alpha^w \rho^w c_p \left( \frac{\partial^w T}{\partial t} + ^w U_i \frac{\partial^w T}{\partial x_i} \right) \\ = \frac{\partial^w q}{\partial x_i} + \bar{H}_{wg} - \underbrace{\bar{H}_{wp}}_{\text{Mean interphase heat transfer (particle-water)}} - \underbrace{H_{wp}^s}_{\text{Subgrid interphase heat transfer (particle-water)}} \\ + \underbrace{\bar{S}}_{\text{Mean field latent heat of vaporization}} + \underbrace{S^s}_{\text{Subgrid latent heat of vaporization}}, \end{aligned} \quad (13)$$

$$\begin{aligned} ^g \alpha^g \rho^g c_p \left( \frac{\partial^g T}{\partial t} + ^g U_i \frac{\partial^g T}{\partial x_i} \right) = \frac{\partial^g q}{\partial x_i} - \bar{H}_{gp} - \bar{H}_{gw} \\ - \underbrace{\bar{S}}_{\text{Mean field latent heat of vaporization}} + \underbrace{S^s}_{\text{Subgrid latent heat of vaporization}}, \end{aligned} \quad (14)$$

and

$$\begin{aligned} ^p \alpha^p \rho^p c_p \left( \frac{\partial^p T}{\partial t} + ^p U_i \frac{\partial^p T}{\partial x_i} \right) = \frac{\partial^p q}{\partial x_i} + \bar{H}_{gp} \\ + \underbrace{\bar{H}_{wp}}_{\text{Mean interphase heat transfer (particle-water)}} + \underbrace{H_{wp}^s}_{\text{Subgrid interphase heat transfer (particle-water)}} \end{aligned} \quad (15)$$

[31] Here the superscripts  $p$ ,  $w$ , and  $g$  refer to the particle, water and gas phases, respectively. Also,  $\alpha$  is volume fraction,  $\rho$  is density,  $T$  is temperature,  $P$  is the pressure,  $\tau_{ij}$  is the stress tensor, and  $U_i$  are the velocity components (for a complete list of variables, see Table 1). Heat transfer between phases is denoted by the  $H$  terms, and the latent heat associated with phase change is given by  $S$ . The rate of steam production is given by  $R_v$ . In the above set of equations, the horizontal brackets denote all terms related to the transfer of heat, mass and momentum caused by production of steam.



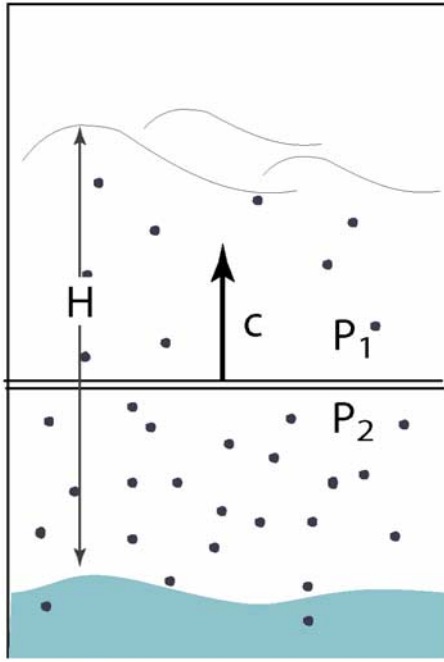


**Figure 8.** Geometry used in the analysis of a critical steam production rate to generate steam explosions (both analytical and numerical model). In the numerical model the particles are all assumed to be 0.1 mm. The sidewalls are free-slip boundaries, and the top is outflow. At the initial time a height ( $H$ ) of pumice is specified and allowed to collapse. In the numerical experiments a specified steam production rate is given at the water surface.  $P_1$  is the initial pressure inside the flow, and  $P_2$  is the pressure behind the characteristic with velocity ( $c$ ).

[32] Heat transfer that results in steam production is primarily accomplished by transfer of thermal energy from the particle phase to the water phase and then into the gas phase. Figure 7 shows schematically the factors related to steam production. Ultimately, the amount of steam production is related to the amount of pumice that reaches the water surface (panel 1). At the water surface steam is produced in the manner described in the experiments (panel 2). As the pumice saturates and sinks it will continue to contribute to the net steam budget only if the mean temperature of the water is at the boiling temperature (panel 3b).

[33] In the developed numerical model, heat transfer and vaporization are composed of two parts: a mean field component and subgrid component. In the model equations the mean interphase heat transfer is given by a standard Nusselt number-based heat transfer coefficient that has been validated for particle Reynolds numbers of  $10^5$  and particle volume fractions from 0 to 0.6 volume fraction [Gunn, 1978; O'Brien and Syamlal, 1991]. The mean field heat transfer reflects a ratio of the time required to transfer thermal energy from the dispersed phase relative to the timescale of the flow. For further discussion of the mean field heat transfer scaling the reader is referred to Dufek and Bergantz [2007].

[34] The mean particle-water heat transfer is given by

$$\bar{H}_{pw} = \gamma_{pw}^0 ({}^pT - {}^wT), \quad (16)$$

where

$$\gamma_{pw}^0 = \frac{6({}^w_{Th}k)({}^p\alpha)Nu}{({}^pd)^2}. \quad (17)$$

[35] Here  ${}^w_{Th}k$  is the thermal conductivity of water and  $Nu$  is the Nusselt number correlation (Table 1).

## 5.2. Proposed Subgrid Model for Water Surface Steam Production

[36] The subgrid heat transfer and phase change model is motivated by the experiments. The primary assumptions used in the development of this model are that (1) all the subgrid-scale heat transfer occurs near the surface of the water, (2) the mass of steam produced for a given amount of particle energy is given by equation (6) from the experiments, and (3) the rate of phase change is given by the mass of steam derived from the experimental relations divided by the time the particle is expected to remain at the surface. The subgrid particle-water heat transfer evaluated at the water-air interface is given as

$$H_{wp}^s = \varepsilon^p \alpha^p \rho^p c_p ({}^pT - {}^wT). \quad (18)$$

[37] Subgrid latent heat release is assumed equal to the subgrid heat transfer:

$$S^s = H_{wp}^s. \quad (19)$$

[38] Finally, the subgrid rate of mass production of steam is given as

$$R_v = \frac{({}^p\alpha)(\varepsilon)({}^p\rho)({}^pc_p)({}^pT - {}^wT)}{\xi m_p [{}^wc_p({}^bT - {}^wT) + L]} = \frac{6({}^p\alpha)(\varepsilon)({}^pc_p)({}^pT - {}^wT)}{\xi \pi d^3 [{}^wc_p({}^bT - {}^wT) + L]}. \quad (20)$$

[39] If the mean temperature of the water exceeds the boiling temperature the rate of vapor production is assumed to be fast enough so that equilibrium conditions are preserved.

## 6. Scaling Argument for Explosive Steam Production

[40] We derive a criterion for explosive steam production events based on the rate of steam generation. We simplify the problem by assuming one-dimensional geometry and we conceptually split the domain by means of a characteristic wave with velocity  $c$  that propagates away from the water surface (Figure 8).

[41] The pressure on both sides of the characteristic wave are specified as  $P_2$  and  $P_1$  and are given by the ideal gas relation.  $P_1$  is the ambient pressure:

$$P_1 = \rho RT. \quad (21)$$



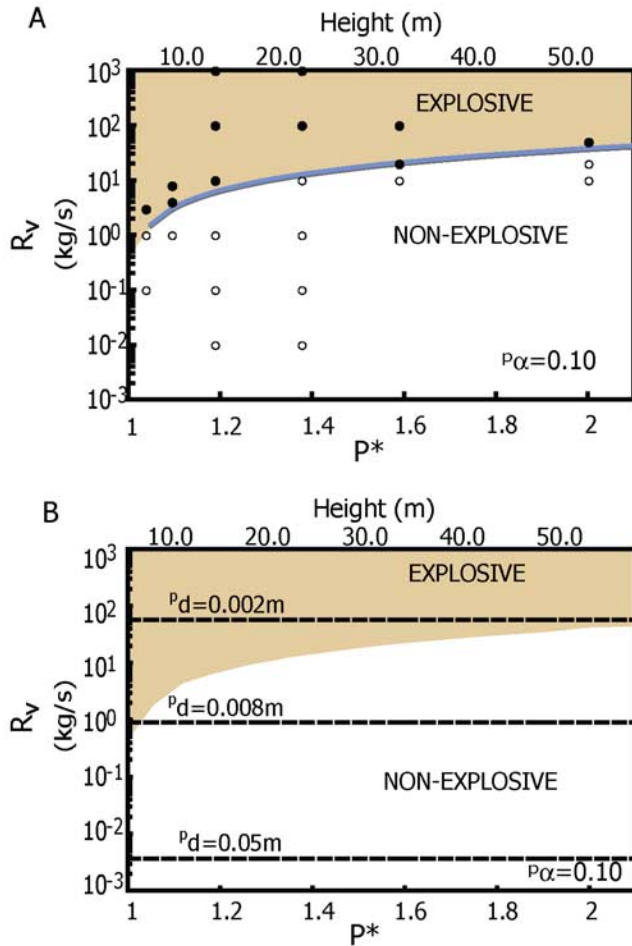


**Figure 9.** Regime diagram of critical steam production rates to produce an explosion. In Figure 9a the solid line is from equation (27). Solid circles denote numerical simulations that resulted in steam explosions, while open circles did not produce shock velocities according to the criteria in equation (27). In Figure 9b the steam explosion regime (shaded area) is compared to the rates predicted by the experimental relation (equation (20)) for a flow with 0.1 volume fraction at 575°C.

[42] The pressure below the characteristic wave is influenced by the production of gas by steam generation.

$$P_2 = \left[ \rho_0 + \frac{R_v}{c} \right] RT. \quad (22)$$

[43] Here  $R_v$  is steam production rate. We treat the characteristic wave as a contact discontinuity whose velocity  $c$  depends on the pressure ratio  $P_2/P_1$  via the Rankine-Hugoniot relations (equation (23)) [Liepmann and Roshko, 1957]. We further specify that  $P_2$  (and hence shock strength) must be equal to or greater than the pressure created by weight of the flow  $P_{flow}$ , so that

$$c = a \left( \frac{\gamma - 1}{2\gamma} + \left[ \frac{\gamma + 1}{2\gamma} \right] \left[ \frac{P_2}{P_1} \right] \right)^{1/2} \quad (23)$$

where  $\gamma$  is the ratio of the gas heat capacities at constant pressure and constant volume, and the critical shock condition is

$$P^* = \frac{P_2}{P_1} \geq \frac{P_{flow} + P_{atm}}{P_{atm}} = \frac{P \rho^p \alpha g H + P_{atm}}{P_{atm}}. \quad (24)$$

[44] In equation (23),  $a$  is the sound speed of the ‘dusty’ gas, given as a function of the temperature and volume fraction of material as [Dobran, 2001]

$$a = \left( \frac{RT_g}{X} \right)^{1/2} \left( X + (1 - X) \frac{\rho_g}{\rho_s} \right), \quad (25)$$

where  $X$  is the gas mass fraction given by

$$X = \left( 1 + \frac{P \alpha^p \rho}{(1 - P \alpha)^g \rho} \right)^{-1}. \quad (26)$$

[45] If we assume that  $R_2 T_2 \approx R_1 T_1$  and taking the ratio of equations (21) and (22) and substituting equation (23) and rearranging terms yields

$$R_v^{\text{critical}} = a \left( \left[ \frac{\gamma - 1}{2\gamma} \right] + \left[ \frac{\gamma + 1}{2\gamma} \right] P^* \right)^{1/2} [P^* - 1]. \quad (27)$$

[46] We also note that in this analysis we assume the particles and gas mixture have a single sound speed. For larger particles, where there is significant gas-particle slip velocity, the analysis will not strictly be correct. Nevertheless, this relation provides guidance on approximating the rates necessary for a steam explosion even for larger particle sizes.

[47] Steam production rates greater than the critical production rate will result in shock overpressures greater than the weight of the flow. From equation (27) we expect that the thicker a pyroclastic flow, the greater the amount of steam production required to create a significant phreatic explosion. We note that at this stage we have defined the critical steam production rate in a way independent from the expected steam production rates given in equation 20 from the experimental measurements.

[48] In order to test this criterion on a number of different flow heights we conducted a series of simulations with a simple geometry depicted in Figure 8, i.e., a collapsing column of particles above a liquid water base. In all these simulations the particle diameter was assumed to be 0.1 mm, and the particles initially have zero velocity. The volume fraction of particles is initially set to 0.1. The top boundary of these simulations is an outflow boundary, and the side boundaries are free slip. Different initial flow heights were considered and are summarized in Figure 9. At the start of the simulations the steam production rate is set at a fixed value. (We stress that in this regime survey we are not using the experimental subgrid model, but fixing the production rate and checking whether a steam explosion occurs.) We determine if the critical shock condition develops in the

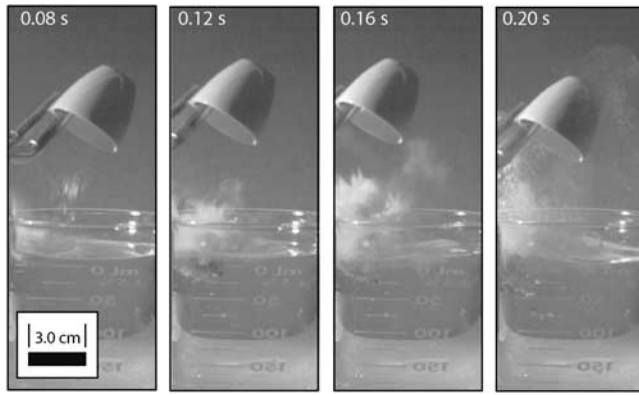


**Figure 10.** Ash at 500°C interacting with water. The ash rapidly generates steam, carrying the fine component outside the beaker.

simulations by scanning through the velocity fields to see if the shock velocity given in equation (23) is achieved. An ensemble of these calculations is combined to form the regime diagram Figure 9.

[49] The simulated steam explosions are in good agreement with the derived steam explosion criterion. At these small particle sizes the gas velocity and the particle velocities are nearly equal, and the assumptions leading to equation (25) are satisfied. In Figure 9b we plot on the regime diagram some example steam production rates from equation (20) given an initial temperature of 575°C and volume fraction of 0.1 and for several different particle diameters. The rate of production of steam is very sensitive to changes in particle diameter when all else is constant. Steam production is inversely proportional to particle mass; hence it is inversely proportional to the cube of the diameter. Our calculations show that for these conditions, particles greater than about a centimeter do not produce steam at sufficiently fast rates to produce a steam explosion, whereas particle size below this can produce steam explosions for these conditions. Changes in the volume fraction of particles, temperature, and flow height will certainly modify the necessary conditions for a steam explosion, but because the steam production rate is only linearly dependent on these quantities, the rate is much more sensitive to changes in particle size. We also note that the experimentally determined steam efficiency ( $\epsilon$ ) and rate constant ( $\xi$ ) are likely dependent on the material properties, including the porosity of the pyroclasts. However, even changing these values 3 orders of magnitude would require only a change in particle diameter by a factor of 10 to produce similar effects.

[50] For very fine particles (<1 mm), water surface tension may also play a role in prolonging the amount of time a particle remains at the water surface. This will enhance the near-surface heat transfer. Measuring the steam production rates of fine particles is not possible using the procedure outlined earlier because a large mass fraction of ash can be carried away during the interaction (Figure 10). We are currently developing a technique to measure ash initiated steam production; however, including the surface

tension effects will likely make the fine particle simulations more explosive than with the current subgrid model.

## 7. Case Example: The 2003 Montserrat Dome Collapse Simulation

### 7.1. The 2003 Montserrat Dome Collapse Event

[51] The 12–13 July 2003 Soufrière Hills dome collapse, and subsequent pyroclastic density current that encountered the sea, is one of the best documented cases of the generation and large-scale dynamics of a littoral blast [Edmonds and Herd, 2005; Edmonds *et al.*, 2006; Mattioli *et al.*, 2007]. We use this event as a template for a series of numerical simulations aimed at understanding the sensitivity of such events to variations in the dynamics and physical characteristics of flows such as flow height and particle grain size distribution. The two-dimensional geometry of the simulations is depicted in Figure 11. This geometry is roughly similar to a two-dimensional representation from the Soufrière Hills lava dome down the Tar River Valley to the sea, although we stress that the aim of these simulations is to delineate the dominant controls on the production of littoral blasts rather than modeling the details of this specific event. For instance, the exact details of the explosion are likely dependent on the initial details of the flow, exact material properties, porosity, in situ fragmentation and change in grain size distribution during the explosion event.

[52] We used the subgrid steam production and heat transfer equations to model the initial entry of pyroclastic flows into the sea. The pyroclastic flow is introduced in a constant flow boundary and then allowed to propagate down the ramp to the sea. The grid has a 15 m horizontal resolution and 10 m vertical resolution throughout the domain. In a sensitivity study, increasing the resolution produced no statistical differences in the flow field, although the fine-scale details of the instabilities are better resolved [Dufek and Bergantz, 2007]. Most of the simulations had only one grain size, although a number of simulations were conducted with two grain sizes in order to examine rudimentary sorting behavior due to the emergent dynamics in the steam explosion and surge.

[53] There are a number of generic flow features associated with simulations that produced steam explosions (Figure 12). Upon reaching the water surface, the flows displace some of the water in the nearshore region, generating a tsunami wave. Contemporaneous heat transfer is assisted by the enhanced interaction of water and pumice in front of the forming wave. The focus of the steam explosion typically nucleates several hundred meters offshore. The rapid steam production associated with the event inflates the pyroclastic flow and in these two-dimensional simulations

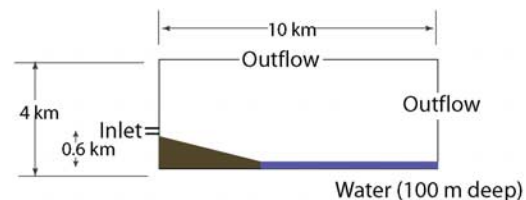


**Figure 11.** Geometry of the numerical simulation domain.

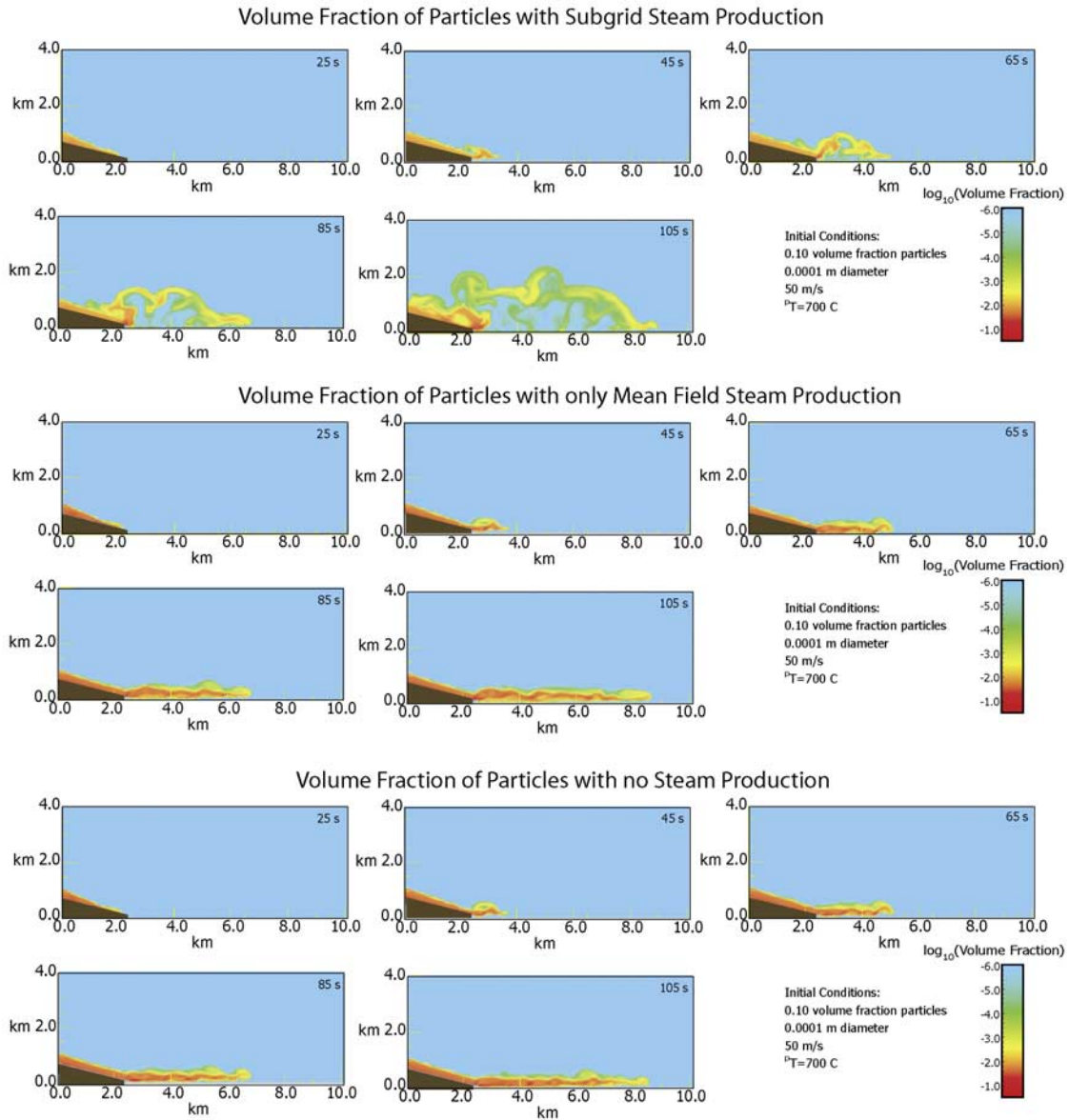


**Figure 12.** Comparison of the temporal evolution of particle volume fraction for simulations with (top) both subgrid and mean steam production, (middle) just mean steam production, and (bottom) no steam production. The inlet feeds the flow with 0.10 volume fraction of 0.1 mm particles traveling at 50 m/s. The flow is initially 700°C.

concentrates the particles in a band between the ambient atmosphere and expanding steam-rich region. The high pressure associated with the steam production also inhibits the propagation of the land-based flow onto the water, concentrating the flow immediately near the shore. A portion of the littoral blast generated by the steam explosion collapses landward and forms an opposing current immediately above the downward propagating flow. Subsequently, some of the more dilute, littoral blast current is mixed back with the land-based flow. In a three-dimensional geometry some of the land-directed current that travels on top of the initiating pyroclastic flow will likely be pushed to either side of pyroclastic flow. As these simulations were conducted in two dimensions we do not access the out of plane expansion of the littoral blast wave.

[54] In all the simulations the surface, subgrid, steam production proved crucial for the generation of a littoral blast when particles sizes were around 0.1 mm. The relative importance of the surface subgrid model versus the production of steam through mean field processes is illustrated in Figures 12 and 13. Figure 12 shows the evolution of volume fraction of particles through time considering (1) the sub-grid, water surface steam production, (2) only mean-field heat transfer and then steam production, and (3) no steam production from the water. These simulations illustrate that while the mean heat transfer does produce some steam the rate of production is much slower, and fails to produce a steam explosion whereas including the subgrid steam generation effect results in vigorous steam production and an explosion. The flow is slightly inflated when only mean



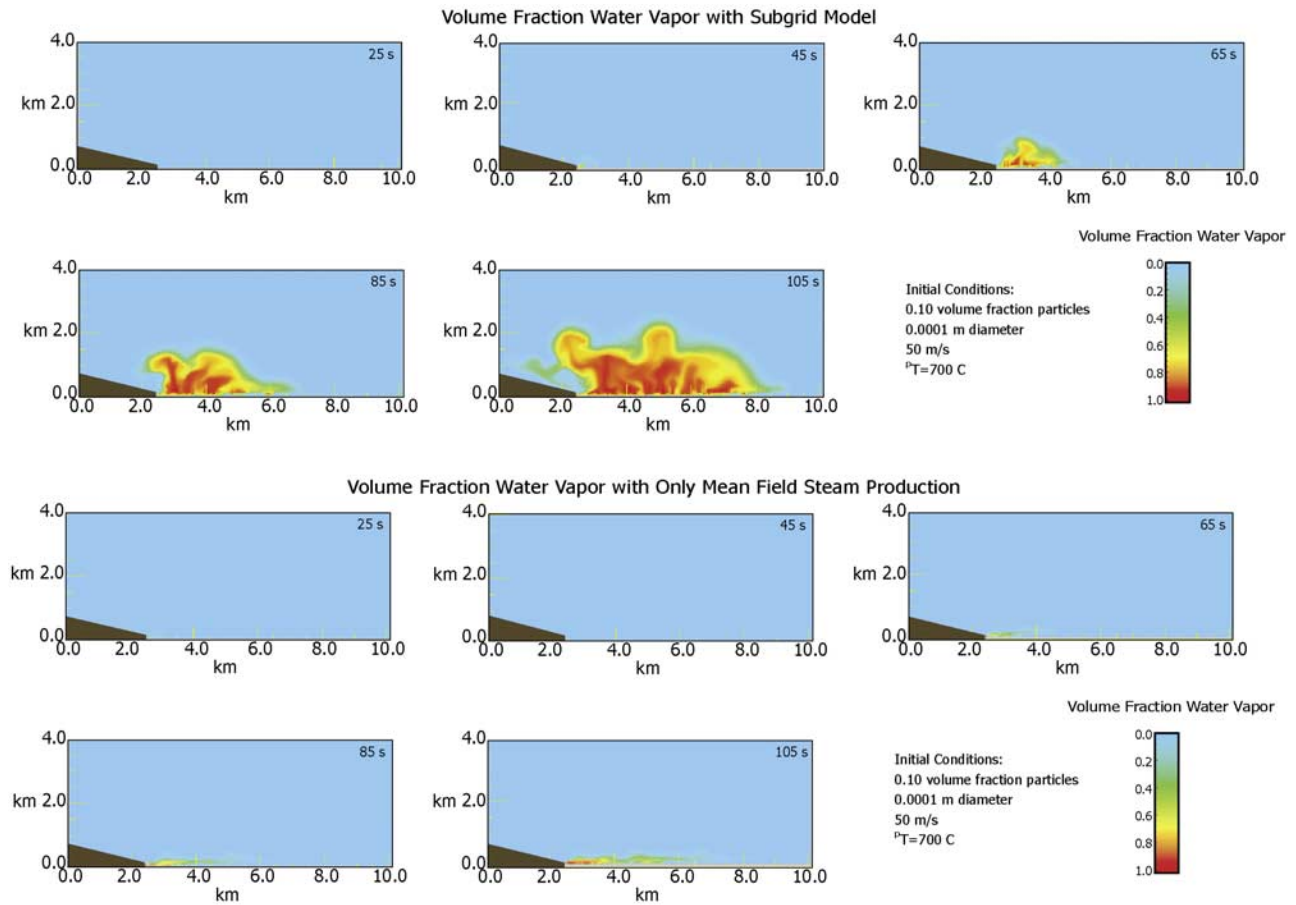


**Figure 13.** A comparison of the temporal evolution of the volume fraction of water vapor generated by (top) subgrid processes and (bottom) mean field processes. Simulation conditions are the same as in Figure 12. Only in the subgrid steam production case is an explosion generated. Although there is a large amount of steam produced, the landward directed base surge is relatively water vapor poor (5–15%) compared to rising plumes.

field steam production is considered relative to no steam production, but qualitatively, these flows are very similar. The amount of steam produced in these two cases is shown in Figure 13. When surface phase change is considered a water vapor enriched region is produced near the water surface, eventually forming buoyant plumes. However, the particle-enriched leading front of the landward directed littoral blast contains only modest amounts of water vapor. The landward directed flow that travels immediately above the initial pyroclastic flow is actually relatively vapor poor with values of 5–15% water vapor. This occurs because the buoyant vapor-rich plumes rise quickly and have relatively little interaction with the near-surface flows. The relatively dry landward directed flow is between  $\sim 200$  and  $500^\circ\text{C}$ , with the upper end of this range occurring near the coast and decreasing as the current cools and entrains air as it propagates.

[55] The analysis used to develop the steam production criterion (Figure 9) showed that the grain size of the particles is likely an important factor in generating a steam explosion. Figure 14 compares two flows, each with the same initial conditions, except that one is composed solely

of 0.1 mm particles and the other is composed of 10.0 mm particles. The flow with the 0.1 mm particles generates a steam explosion as previously described, whereas the 10.0 mm particle flow fails to produce steam at a fast enough rate to generate an explosion. Instead, the flow with the larger particles is inflated by the steam produced by roughly a factor of 2, but because it does not generate an explosion very little material is forced landward. The higher settling velocity of the larger particles also results in very low height, basally concentrated flows compared to the 0.1 mm flows.

[56] The flow height (and hence the pressure at the base of the flow) should also have some control on the generation of steam explosions. To test this, flows composed of 0.1 mm particles of different initial height were examined (Figure 15). Initial flow heights of 200, 400, and 900 m were examined. In all three cases the flows have developed vertical gradients in particle concentration as they traveled down the ramp by the time they reach the water. The two smaller height flows produce a steam explosion with a component of the flow forming a landward directed blast,



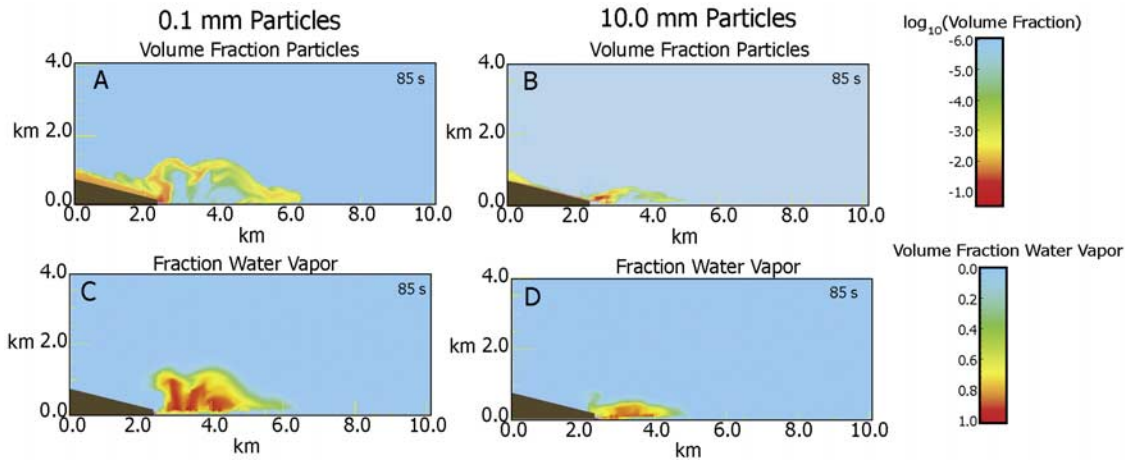


**Figure 14.** Comparison of flows composed of 0.1 mm particles and 10.0 mm particles (85 s). (top) Volume fraction of particles (log scale) and (bottom) volume fraction of water vapor. The 10.0 mm particle flow develops into a basally concentrated flow, and the particles fail to initiate a steam explosion.

whereas the largest of these flows, while it does inflate due to steam generation, fails to produce a littoral blast.

[57] We investigated rudimentary sorting that results from littoral blasts by simulating flows with two particle sizes. In these simulations, 50% of the flow is composed initially of 0.1 mm particles and 50% 1.0 mm particles. An example simulation is shown in Figure 16. Although both the 0.1 mm and 1.0 mm particles are concentrated above the steam enriched regions, the landward directed base surge contains ~10 times the amount fine (0.1 mm) particles relative to 1.0 mm particles. The 1.0 mm particles preferentially enter the water compared to the 0.1 mm particles and are more diffusely distributed in the steam enriched region.

[58] Steam explosions generated by the fine component of more complex particle size distributions can be assessed with similar scaling arguments presented in equations (20)–(27). If we assume that the smallest particles contribute all the steam over the timescale of shock development, and the larger particles contribute no steam (but do contribute to the overburden of the overlying flow, equations (20) and (27) can be combined to give the following expression:

$$p_{\alpha_1} \geq \frac{\xi \pi d^3 [w c_p (b T - w T) + L]}{6(\varepsilon) (p c_p) (p T - w T)} a \left\{ \left[ \frac{\gamma - 1}{2\gamma} \right] + \left[ \frac{\gamma + 1}{2\gamma} \right] P^* \right\}^{1/2} \cdot [P^* - 1]. \quad (28)$$

[59] Here  $p_{\alpha_1}$  is the volume fraction of small particles, and the sound speed of the dusty gas ( $a$ , equation (25)) and the overpressure ratio ( $P^*$ , equation (24)) are functions of the total particle volume fraction. This is a simplification because (1) the thermal energy of larger particles will contribute to the production of some steam during the shock production and (2) the assumption that the particles and the gas are well coupled in estimating the dusty gas sound speed will not be accurate for larger particles. Particles with aerodynamic response times much greater than the timescale of the shock passing the particle will likely not accelerate significantly from their previous course (Figure 16). Nevertheless, equation (28) does give some

intuition as to the relative proportions of fines that are required to produce a steam explosion. For a 200 m thick flow, with total particle volume fraction of 0.1, at 500°C, only 0.02% of the flow needs to be 0.1 mm or smaller to produce enough steam to balance the overburden pressure of the flow. If the fine component is 1.0 mm particles, ~20% of the flow must be composed of these particles. If the smallest particles in a flow are 10.0 mm a steam explosion does not develop. We stress again, that even if

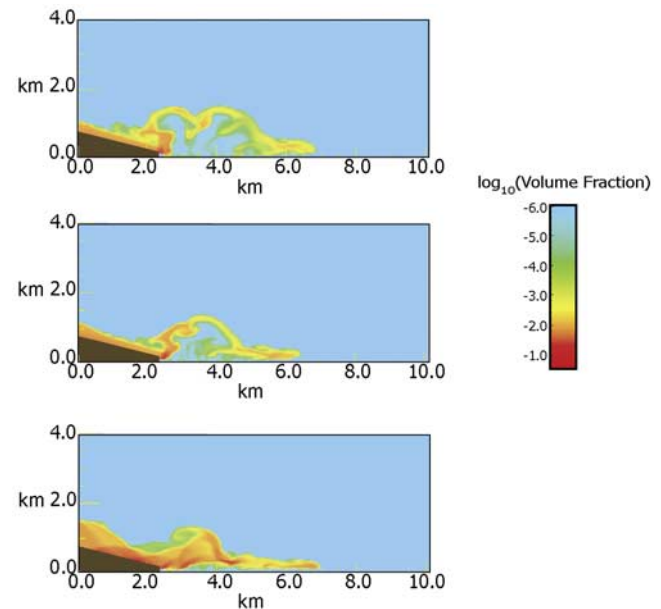


**Figure 15.** Effect of flow height (flow overpressure) on the development of littoral blasts. Initial flow heights are 200, 400, and 900 m, respectively, and initial flow concentration is 0.1 volume fraction of particles. All flows contain 0.1 mm particles and are initially 700°C. The 200 and 400 m flows produce a landward directed base surge, whereas the 900 m flow inflates but does not produce a landward base surge.

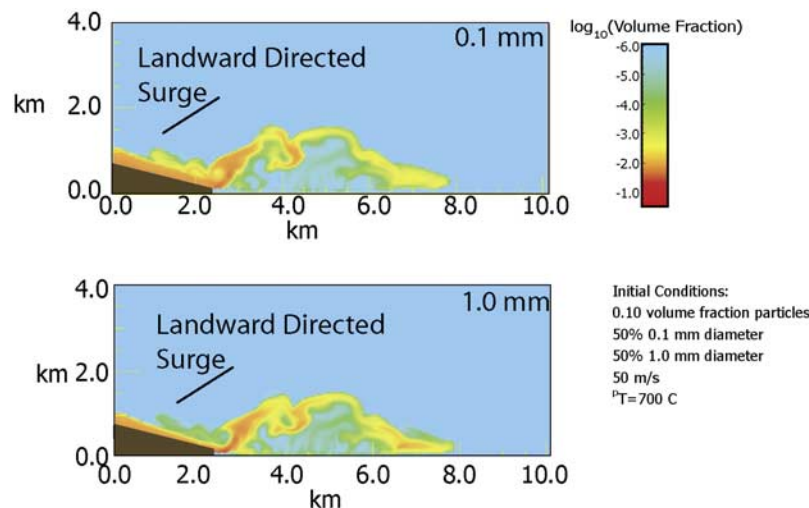


**Figure 16.** Sorting generated by a littoral blast (90 s). The simulated flows initially contain 0.10 volume fraction of particles (50% 0.1 mm and 50% 1.0 mm). The 0.1 mm particles are preferentially concentrated in the landward directed base surge. Relative to the 0.1 mm particles the 1.0 mm particles are more diffusely distributed in the steam enriched regions.

a steam explosion does occur it will only preferentially carry with it the fine particles as is shown in Figure 16.

## 7.2. Comparison to Observed Deposits of the 12–13 July Event

[60] Although three-dimensional effects played an important role in the distribution of deposits of the 12–13 July littoral blast (Irish Ghaut facies), several comparisons can be made with the interpreted littoral blast deposits [Edmonds *et al.*, 2006] and these simulations. On the basis of the prevalence of large glassy blocks (>16 mm) from the dome collapse, Edmonds *et al.* [2006] hypothesized that these blocks fragmented on contact with water producing a finer grain mixture, which allowed the water to be heated more quickly, generating a steam explosion. Although we do not consider the effect of secondary hydrofragmentation, the results of these numerical simulations are consistent with the fine material initiating the steam explosion. The mean grain sizes measured in the Irish Ghaut facies were between 0.5 and 0.06 mm and are consistent with the size of particles small enough to rapidly generate steam (Figure 9). Likewise, grain size distributions of past dome collapse events of the Soufrière Hills dome produced median diameter of between 0.3 and 3.0 mm, within the range of expected of particles able to produce rapid steam generation [Cole *et al.*, 2002]. The observation of scorched plant material led Edmonds *et al.* [2006] to interpret these flows as hot and relatively dry, which is also consistent with the numerical simulations. In addition the simulations predict that accretionary lapilli, generated in a steam rich environment, would likely develop in the area immediately above the blast zone, and seaward of most of the landward directed base surge.

[61] In order to compare relative volumes of material that composed the landward directed base surge, we chose a flow with initially 0.1 volume fraction particles that is 200 m high as our reference simulation. Overflow from the Tar River Valley indicated that the initial pyroclastic flows were greater than 80 m in height. Likewise we used the grain size

of 0.1 mm that is in the range of average grain size reported in the landward base surge. The cumulative flux at a station 400 m inland is shown in Figure 17. At this location, ~94% of the simulated flow eventually passed headed toward the sea and ~0.6% volume of the flow formed the landward directed base surge. A remaining ~5% of the simulated flow is deposited on the slopes before reaching this location. Edmonds *et al.* [2006] estimated that the volume of the interpreted base surge was ~0.75% ( $1.5 \times 10^6 \text{ m}^3$ ) compared to the total dome collapse volume.

[62] The near simultaneous generation of a tsunami (recorded by tide gauge) and the blast (noted by the cutoff of data from a remote video camera) are also consistent with the numerical simulations [Edmonds and Herd, 2005; Mattioli *et al.*, 2007]. It should also be noted that blast cones were not observed on beach from the 12–13 July event. Although not definitive, this does support the interpretation, as seen in the simulations, that the main portion of the blast was generated a few hundred meters offshore.

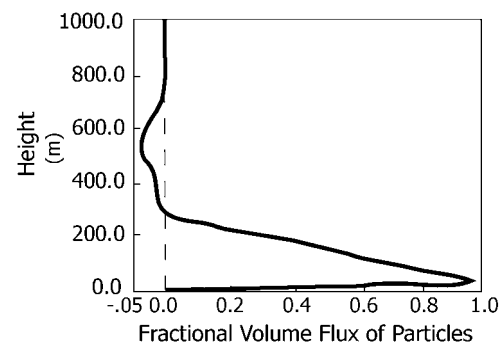


**Figure 17.** Total flux measured at 2000 m (400 m inland of the simulated shoreline). The simulated flow had 0.1 volume fraction and was initially 200 m high. The negative values above ~300 are the result of the landward directed base surge event.

Mattioli *et al.* [2007] considered a displacement volume of  $7 \times 10^6 \text{ m}^3$  at 70 m/s to model the tsunami produced when pyroclastic flow material enters the water. The Mattioli *et al.* [2007] simulations with these conditions produced wave heights that were smaller than expected for the observed maximum strain amplitude of the broadband seismometer measurements, and these authors suggest that either a greater volume or more energetic currents produced the tsunami waves. The velocity of the basal region of our simulated current was 70–80 m/s at the shoreline and was slightly more energetic than the tsunami simulation conditions considered by Mattioli *et al.* The steam explosion may also provide some of the extra energy required to produce larger tsunamis.

## 8. Conclusions

[63] The rate at which heat is transferred from hot pyroclasts to water ultimately determines whether a steam explosion will be generated when pyroclastic flows reach the sea. Laboratory measurements of single-pumice heat transfer indicate that pumice-water heat transfer near the water surface may play a crucial role in quickly generating steam, with  $\sim 10\%$  of the thermal energy of a particle contributing to steam production. The experiments showed that the rate of steam production was also very sensitive to particle size, varying inversely as the cube of the particle diameter. Buildup of steam-generated pressures greater than the basal pressure of a pyroclastic flow requires grain sizes typically less than about 1–5 mm.

[64] A self-consistent set of subgrid heat transfer and steam production equations was developed in the context of multiphase flow continuum theory based on the laboratory measurements. The model was applied to a situation analogous to the 12–13 July Soufrière Hills dome collapse event. Our analysis revealed that grain sizes of  $\sim 0.1 \text{ mm}$  and initial flow heights of  $\sim 200 \text{ m}$  produced volumes and dynamics similar to those inferred by the deposits of the landward directed base surge. Simulated flows thicker than  $\sim 800 \text{ m}$  and with grain sizes over 1 cm in the same geometry do not produce steam explosions. The simulations also indicated that the landward directed base surges will likely preferentially transport finer material and are relatively water vapor poor. However, just seaward of the coast a water vapor rich region forms that sources buoyant plumes. The water vapor rich plumes may be a likely site for the development of accretionary lapilli as the vapor begins to recondense on the particles in the energetic plumes.

[65] **Acknowledgments.** We thank Glen Mattioli, Christian Huber, an anonymous reviewer, and Associate Editor John Spray for their helpful comments and discussion of this manuscript. This work was supported by a Miller Institute Research Fellowship (J.D.) and NSF grant EAR-0408312 (M.M. and M.S.).

## References

- Agrawal, K., *et al.* (2001), The role of meso-scale structures in rapid gas-solid flows, *J. Fluid Mech.*, **445**, 151–185.
- Allen, S. R., and R. A. F. Cas (2001), Transport of pyroclastic flows across the sea during explosive, rhyolitic eruption of the Kos Plateau Tuff, Greece, *Bull. Volcanol.*, **62**, 441–456.
- Brouillette, M. (2002), The Richtmyer-Meshkov instability, *Annu. Rev. Fluid Mech.*, **34**, 445–468.
- Bye, J. A. T. (1995), Inertial coupling of fluids with large density contrast, *Phys. Lett. A*, **202**, 222–224.
- Cagnoli, B., and M. Manga (2004), Granular mass flows and Coulomb's friction in shear cell experiments: Implications for geophysical flows, *J. Geophys. Res.*, **109**, F04005, doi:10.1029/2004JF000177.
- Carey, S., *et al.* (1996), Pyroclastic flows and surges over water: An example from the 1883 Krakatau eruption, *Bull. Volcanol.*, **57**, 493–511.
- Cashman, K. V., and R. V. Fiske (1991), Fallout of pyroclastic debris from submarine volcanic eruptions, *Science*, **253**, 275–280.
- Cole, P. D., *et al.* (2002), Deposits from dome-collapse and fountain-collapse pyroclastic flows at Soufrière Hills Volcano, Montserrat, in *The Eruption of Soufrière Hills Volcano, Montserrat From 1995 to 1999*, edited by T. H. Druitt and B. P. Kokelaar, *Mem. Geol. Soc.*, **21**, 231–262.
- Dartevelle, S., W. I. Rose, J. Stix, K. Kelfoun, and J. W. Vallance (2004), Numerical modeling of geophysical granular flows: 2. Computer simulations of Plinian clouds and pyroclastic flows and surges, *Geochem. Geophys. Geosyst.*, **5**, Q08004, doi:10.1029/2003GC000637.
- Dobran, F. (2001), *Volcanic Processes, Mechanisms in Material Transport*, 590 pp., Kluwer Acad. Norwell, Mass.
- Dufek, J. D., and G. W. Bergantz (2005), Transient two-dimensional dynamics in the upper conduit of a rhyolitic eruption: A comparison of the closure models for the granular stress, *J. Volcanol. Geotherm. Res.*, **143**, 113–132.
- Dufek, J. D., and G. W. Bergantz (2007), The suspended-load and bed-load transport of particle laden gravity currents: Insight from pyroclastic flows that traverse water, *Theoret. Comput. Fluid Dyn.*, **21**, 119–145.
- Edmonds, M., and R. A. Herd (2005), Inland-directed base surge generated by the interaction of pyroclastic flows and seawater at Soufrière Hills volcano, Montserrat, *Geology*, **33**, 245–248.
- Edmonds, M., *et al.* (2006), Tephra deposits associated with a large lava dome collapse, Soufrière Hills Volcano, Montserrat, 12–15 July 2003, *J. Volcanol. Geotherm. Res.*, **153**, 313–330.
- Fisher, R. V., *et al.* (1993), Mobility of a large-volume pyroclastic flow-emplacment of the Campanian ignimbrite, Italy, *J. Volcanol. Geotherm. Res.*, **56**, 262–275.
- Freundt, A. (2003), Entrance of hot pyroclastic flows into the sea: Experimental observation, *Bull. Volcanol.*, **65**, 144–164.
- Gera, D., *et al.* (2004), Hydrodynamics of particle segregation in fluidized beds, *Int. J. Multiphase Flow*, **30**, 419–428.
- Grove, T. L., and J. M. Donnelly-Nolan (1986), The evolution of young silicic lavas at Medicine Lake Volcano, California—Implications for the origin of compositional gaps in calc-alkaline series lavas, *Contrib. Mineral. Petrol.*, **92**, 281–302.
- Grunewald, U., *et al.* (2007), MFCI experiments on the influence of NaCl-saturated water on phreatomagmatic explosions, *J. Volcanol. Geotherm. Res.*, **159**, 126–137.
- Gunn, D. J. (1978), Transfer of heat or mass to particles in fixed and fluidized beds, *Int. J. Heat Mass Transfer*, **21**, 467–476.
- Kandlikar, S. G., and P. Balasubramanian (2005), An experimental study on the effect of gravitational orientation on flow boiling of water in  $1054 \times 197$  micrometer parallel minichannels, *J. Heat Transfer*, **127**, 820–829.
- Klug, C., and K. V. Cashman (1996), Permeability development in vesiculating magmas: Implications for fragmentation, *Bull. Volcanol.*, **58**, 87–100.
- Kundu, P. K. (1990), *Fluid Mechanics*, 638 pp., Academic, San Diego, Calif.
- LaCroix, A. (1904), *La Montagne Pelee et ses eruptions*, Masson, Paris.
- Liepmann, H. W., and A. Roshko (1957), *Elements of Gas Dynamics*, 439 pp., John Wiley, New York.
- Manville, V., *et al.* (2002), Hydrodynamic behavior of Taupo 1800a pumice; implications for the sedimentology of remobilized pyroclasts, *Sedimentology*, **49**, 955–976.
- Mattioli, G. S., *et al.* (2007), Unique and remarkable dilatometer measurements of pyroclastic flow-generated tsunamis, *Geology*, **35**, 25–28.
- Muller, S. O., *et al.* (2005), Permeability and degassing of dome lavas undergoing rapid decompression: An experimental determination, *Bull. Volcanol.*, **67**, 526–538.
- Neri, A., *et al.* (2002), Mass partition during collapsing and transitional columns by using numerical simulations, *J. Volcanol. Geotherm. Res.*, **115**, 1–18.
- O'Brien, T. J., and M. Syamlal (1991), Fossil Fuel Circulating Fluidized Bed: Simulation and Experiment, in *Advances in Fluidized Systems*, edited by E. L. Gaden and A. W. Weimer, *AIChE Symp. Ser.*, **281**, 127–136.
- Rust, A. C., and K. V. Cashman (2004), Permeability and degassing of dome lavas undergoing rapid decompression: An experimental determination, *Bull. Volcanol.*, **67**, 526–538.
- Saar, M. O., and M. Manga (1999), Permeability-porosity relationship in vesicular basalts, *Geophys. Res. Lett.*, **26**, 111–114.
- Sigurdsson, H., S. Cashdollar, and R. S. J. Sparks (1982), The eruption of Vesuvius in A. D. 79: Reconstruction from historical and volcanological evidence, *Am. J. Archaeol.*, **86**, 39–51.

- Stebbins, J. F., et al. (1984), Heat-capacities and entropies of silicate liquids and glasses, *Contrib. Mineral. Petrol.*, 86, 131–148.
- Taylor, P. A., and P. R. Gent (1978), A numerical investigation of variations in the drag coefficient for air flow above water waves, *Q. J. R. Meteorol. Soc.*, 104, 979–988.
- Watts, P., and C. F. Waythomas (2003), Theoretical analysis of tsunami generation by pyroclastic flows, *J. Geophys. Res.*, 108(B12), 2563, doi:10.1029/2002JB002265.
- Whitham, A. G., and R. S. J. Sparks (1986), Pumice, *Bull. Volcanol.*, 48, 209–223.
- Wohletz, K. H. (1986), Explosive magma-water interactions; thermodynamics, explosive mechanisms and field studies, *Bull. Volcanol.*, 48, 245–264.
- Zabrodsky, S. S. (1963), A note on the heat transfer between spherical particles and a fluid in a bed, *Int. J. Heat Mass Transfer*, 6, 991–997.
- Zimanowski, B., et al. (1997), Premixing of magma and water in MFCI experiments, *Bull. Volcanol.*, 58, 491–495.
- 
- J. Dufek, M. Manga, and M. Staedter, Department of Earth and Planetary Science, University of California, 307 McCone Hall, Berkeley, CA 94720-4768, USA. (dufek@berkeley.edu)